Nanoscale

PAPER

View Article Online
View Journal

Cite this: DOI: 10.1039/d5nr02166a

Thermal conversion of metal hydroxide acrylate nanoparticles immobilized on TiO_2 toward noble-metal-free photocatalytic H_2 production

Naoki Tarutani, *[a] Rei Nitomakida,[a] Kiyofumi Katagiri, [a] Kei Inumaru, [a] Sayako Inoué, [b] Hiroki Yamada, [c] Toshiaki Ina[c] and Yousuke Ooyama *[a]

Developing efficient and noble-metal-free photocatalysts for hydrogen evolution is a central challenge in solar fuel production. Herein, we report a strategy to enhance the photocatalytic activity of rutile TiO_2 by immobilising nickel hydroxide acrylate (NHA) nanoparticles, which serve as thermally convert cocatalyst precursors. Upon heat-treatment under an Ar atmosphere, the NHA nanoparticles decompose to form a composite nanostructure comprising sub-10 nm Ni/NiO_x and carbon nanodomains. The optimised hybrid system exhibited a 37-fold increase in photocatalytic H_2 evolution activity compared to pristine TiO_2 under UV light irradiation. Analysis of band edge potentials revealed a downward shift in the conduction band minimum, facilitating more efficient reduction processes. In contrast, a control sample prepared using $Ni(NO_3)_2$ resulted in inactive NiO_x domains and poor interfacial bonding, leading to suppressed activity. These findings demonstrate that NHA-derived cocatalysts provide a versatile platform for constructing noble-metal-free photocatalytic systems through controlled interfacial nanostructuring, offering new avenues for designing advanced solar-to-fuel materials.

Received 22nd May 2025,
Accepted 4th September 2025

DOI: 10.1039/d5nr02166a

rsc.li/nanoscale

Introduction

The increasing global demand for energy, coupled with the urgent imperative to address climate change, has driven the pursuit of clean and sustainable energy technologies. Among them, H_2 stands out as a carbon-neutral fuel with high energy density, positioning it as a key player in the transition to a decarbonised energy system. Photocatalytic water splitting, which harnesses solar energy to decompose water into H_2 and O_2, offers an environmentally benign and resource-abundant approach to H_2 production.[1–3] Since the seminal demonstration by Fujishima and Honda of photoelectrochemical water splitting using a single-crystal rutile TiO_2 photoanode under ultraviolet (UV) irradiation and applied bias,[4] the field has witnessed remarkable progress. Beyond the development of efficient photocatalysts, the design of cocatalysts plays a pivotal role in promoting charge separation and surface redox reactions. Indeed, external quantum efficiencies of ~96% have been achieved in overall water splitting systems by facet selective deposition of Rh/Cr_2O_3 (for H_2 evolution) and CoOOH (for O_2 evolution) cocatalysts.[5] Cocatalysts are typically engineered at the sub-10 nm scale to maximise surface area and minimise light-shielding effects. In this context, various materials including Ru,[6] Rh/Cr_2O_3,[7] RuO_x,[8] IrO_x,[9,10] CoO_x,[11,12] have proven essential for facilitating the H_2 and O_2 evolution reactions when integrated with diverse photocatalytic systems. A persistent challenge, however, lies in expanding the compositional and structural diversity of cocatalysts while eliminating noble metals—an objective that remains difficult due to the size requirements.

In the present study, we introduce a strategy that employs metal hydroxide salt (MHS) nanoparticles as precursors for cocatalyst formation. MHS, also known as layered hydroxide salts,[13,14] are capable of incorporating a diverse range of metal cations homogeneously at the atomic level. They can be represented by the general formula $M(OH)_{2-x}(A^{m-})_{x/m}{\cdot}nH_2O$ (M = Co^{2+}, Ni^{2+}, Cu^{2+}, Zn^{2+}, *etc.* and A = Cl^-, SO_4^{2-}, carboxylates, *etc.*).[13,14] Such materials, which possess molecular units within their crystal structures, referred to as "supra-ceramics", have attracted significant attention.[15] We previously reported a solution-based method for synthesising monolayer MHS nanoparticles with a diameter of ~2 nm, which provides precise control over their composition and morphology.[16] Notably, heat-treatment of these nanoparticles has been shown to

[a]*Applied Chemistry Program, Graduate School of Advanced Science and Engineering, Hiroshima University, 1-4-1 Kagamiyama, Higashi-Hiroshima, Hiroshima 739-8527, Japan. E-mail: n-tarutani@hiroshima-u.ac.jp, yooyama@hiroshima-u.ac.jp*
[b]*Geodynamics Research Center (GRC), Ehime University, Matsuyama 790-8577, Japan*
[c]*Japan Synchrotron Radiation Research Institute, 1-1-1 Kouto, Sayo-Cho, Sayo-Gun, Hyogo, 679-5198, Japan*

induce thermal conversion of MHS nanoparticles, yielding either metals/alloys[17] or a variety of inorganic compounds (carbides, nitrides, sulphides, phosphides, *etc.*),[18] depending on the processing conditions. Owing to their compositional versatility and tunable phase evolution, thermally converted MHS nanoparticles represent a promising platform for the development of novel cocatalyst materials—particularly those beyond the scope of conventional systems reported to date.

Results and discussion

Rutile-phase TiO_2 was selected as the photocatalyst in this study due to its well-documented capability to promote overall water splitting under UV irradiation.[19,20] Commercial TiO_2 powder (JRC-TIO-16, Catalysis Society of Japan) was pre-treated at 873 K for 2 h in air, hereafter referred to as pristine-TiO_2. Cocatalyst immobilisation was achieved by dispersing the pristine-TiO_2 in a colloidal solution of nickel hydroxide acrylate (NHA) nanoparticles, prepared according to our previous protocol,[16,21] with a nominal TiO_2 : Ni weight ratio of 0.98 : 0.02. The resulting homogeneous suspension was dried at 353 K, followed by thermal treatment at 873 K for 1 h under an argon atmosphere to yield the NHA-TiO_2 sample. For comparison, a control sample (NN-TiO_2) was prepared by suspending pristine-TiO_2 in an aqueous $Ni(NO_3)_2$ solution, drying, and heat-treating under identical conditions. Photocatalytic water splitting was conducted in a Pyrex top-irradiation vessel connected to a closed gas circulation system, as described in previous studies.[19,20] The photocatalysts (pristine-TiO_2, NHA-TiO_2, and NN-TiO_2) were suspended in aqueous solution containing 10 vol% methanol as a sacrificial agent. Irradiation was provided by a 300 W xenon lamp (output current: 20 A), and evolved gases were quantified using gas chromatography (Shimadzu, GC-8A). As shown in Fig. 1, H_2 evolution was observed in both the pristine-TiO_2 and NHA-TiO_2 systems, with the amount increasing proportionally with irradiation time. In contrast, no H_2 generation was detected for NN-TiO_2. The average H_2 evolution rate for pristine-TiO_2 was 1.7 μmol h^{-1}, whereas NHA-TiO_2 exhibited a markedly enhanced rate of 63.4 μmol h^{-1}—a 37-fold increase. These results indicate that the photocatalytic activity of rutile TiO_2 was significantly enhanced by the NHA-derived cocatalyst, while being suppressed by the $Ni(NO_3)_2$-derived counterpart. NiO_x has long been reported as an effective cocatalyst for overall water splitting on TiO_2, primarily due to suppression of the backward reaction.[22] In our experiments, however, stoichiometric overall water splitting was not achieved with the NHA-TiO_2 system, despite its significantly enhanced hydrogen evolution activity. This discrepancy suggests that the actual cocatalyst structure may differ from the conventional core–shell NiO_x configuration. Therefore, further characterisation was undertaken to elucidate the origins of this contrasting behaviour.

Synchrotron X-ray diffraction (XRD) patterns of pristine-TiO_2, NHA-TiO_2, and NN-TiO_2 reveal the formation of $NiTiO_3$ in the NN-TiO_2 sample in addition to rutile phase TiO_2 (Fig. 2), suggesting a solid-state reaction between immobilised $Ni(NO_3)$ and the TiO_2 matrix during thermal treatment. In contrast, the XRD patterns and calculated lattice parameters/crystallite sizes of pristine-TiO_2 and NHA-TiO_2 were almost identical (Table S1), indicating that no significant structural change, such as Ni doping into the TiO_2 lattice, occurred in the NHA-TiO_2 system. Further morphological and compositional analysis was conducted using scanning electron microscopy (SEM), transmission electron microscopy (TEM), scanning transmission electron microscopy (STEM), and STEM-energy dispersive spectroscopy (EDS) mapping. The pristine-TiO_2 particles exhibited diameters of approximately 35 nm with dis-

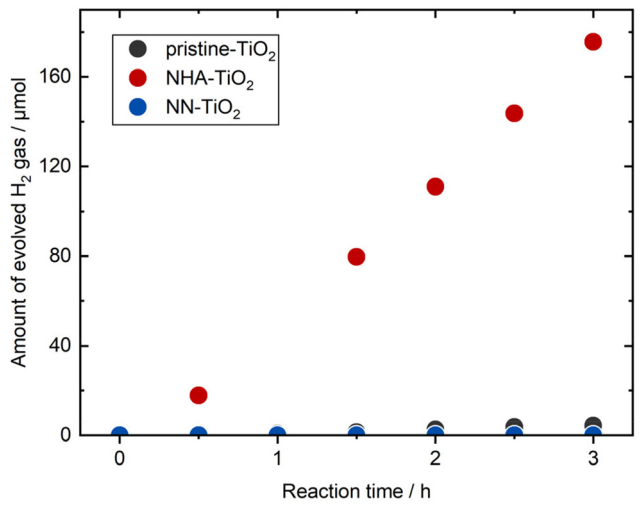

Fig. 1 Time courses of H_2 evolution from an aqueous solution containing 10 vol% methanol on pristine-TiO_2 (black), NHA-TiO_2 (red), and NN-TiO_2 (blue) under UV irradiation.

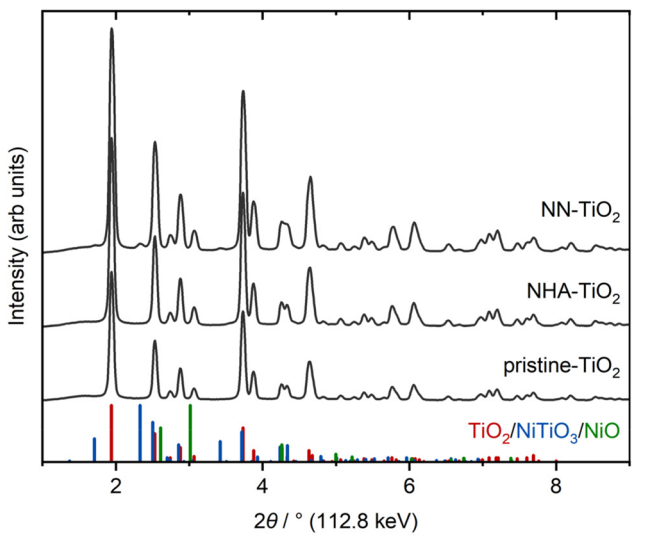

Fig. 2 Synchrotron XRD patterns of pristine-TiO_2, NHA-TiO_2, and NN-TiO_2. The bars indicate peak positions of rutile phase TiO_2 (red, JCPDS #21-1276), $NiTiO_3$ (blue, #33-0960), and NiO (green, #44-1159).

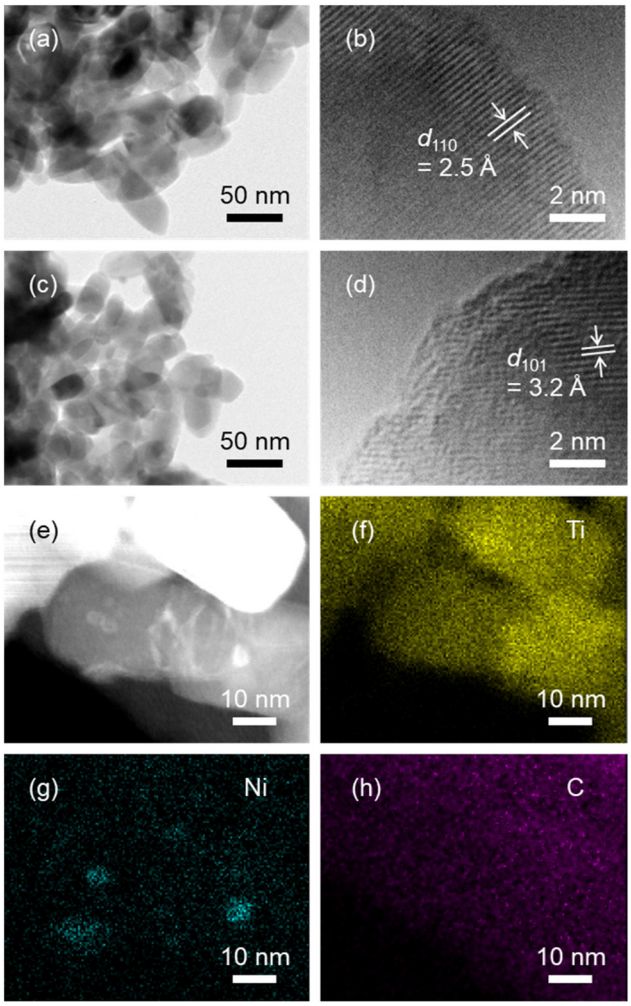

Fig. 3 (a)–(d) TEM images of (a) and (b) pristine-TiO_2 and (c) and (d) NHA-TiO_2. (e) STEM image, and EDS elemental maps of (f) Ti, (g) Ni and (h) C of NHA-TiO_2.

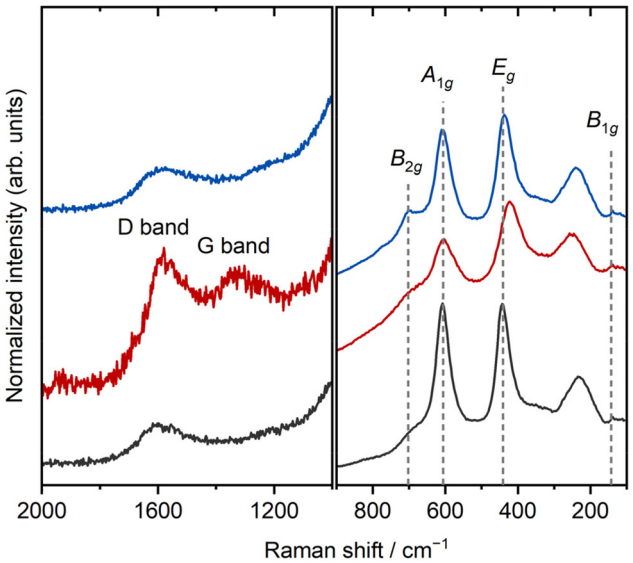

Fig. 4 Raman spectra of pristine-TiO_2 (black), NHA-TiO_2 (red), and NN-TiO_2 (blue).

tinct surface lattice fringes (Fig. 3a, b, and S1a), indicative of high crystallinity. NHA-TiO_2 particles showed similar dimensions (Fig. 3c and S2b); however, surface amorphous layers approximately 2–3 nm thick were partially observed (Fig. 3d). STEM–EDS mapping (Fig. 3e–h) and TEM/STEM-EELS observations (Fig. S2) revealed the presence of Ni species on the TiO_2 surface, with an average particle size of 14.0 nm. Although some aggregation of Ni species likely occurred during thermal treatment considering the size of the precursor NHA nanoparticles (~2 nm), the Ni-containing domains remained within the sub-10 nm regime. These STEM and EDS observations are consistent with the XRD results, supporting the conclusion that Ni species were deposited on the TiO_2 surface without incorporation into the lattice, thereby ruling out Ni doping as the primary mode of interaction.

The Raman spectrum of pristine-TiO_2 exhibits prominent peaks at 138, 230, 441, and 608 cm^{-1} (Fig. 4), corresponding to the B_{1g}, multi-photon process, E_g, A_{1g}, and B_{2g} vibrational modes, respectively.[23] In contrast, the E_g mode of NHA-TiO_2 is markedly red-shifted to 420 cm^{-1} and exhibits a broader full width at half maximum (34 cm^{-1} for pristine-TiO_2 and 55 cm^{-1} for NHA-TiO_2). Suggesting the formation of an amorphous phase and/or the introduction of oxygen-related defects.[24,25] X-ray photoelectron spectroscopy (XPS) and X-ray absorption fine structure (XAFS) analyses confirmed that the oxidation state of Ti remained at +4 before and after heat-treatment (Fig. S3), indicating that the observed spectral changes are primarily attributable to amorphization rather than oxygen defect formation. Additionally, NHA-TiO_2 displays characteristic Raman bands at 1323 and 1582 cm^{-1}, corresponding to the D and G bands of graphitic carbon species.[26,27] This observation aligns with previous reports demonstrating that NHA nanoparticles undergo thermally induced self-reduction, yielding metallic Ni through a Ni_3C intermediate, accompanied by carbon phase segregation.[17,28] The XPS spectra of the C 1s region were comparable between pristine-TiO_2 and NHA-TiO_2 (Fig. S3(c)). This indicates that the amount of carbon species thermally formed during the conversion of NHA nanoparticles is small, making it difficult to extract detailed information from the spectra. This interpretation is also supported by the STEM-EDS mapping (Fig. 3(h)), in which only a weak and spatially diffuse C signal was observed. The presence of carbon on TiO_2 surfaces has been shown to enhance photocatalytic performance,[29,30] potentially by facilitating shallow trapping of photogenerated electrons at oxygen vacancy sites *via* interfacial interactions between carbon and TiO_2. When NHA–TiO_2 was prepared using different dispersion media (water, ethanol, and acetone), the rates of H_2 evolution were comparable (Fig. S4). This result indicates that the present preparation process exhibits good reproducibility.

The chemical states of the nickel species were investigated using the X-ray absorption near-edge structure (XANES) of

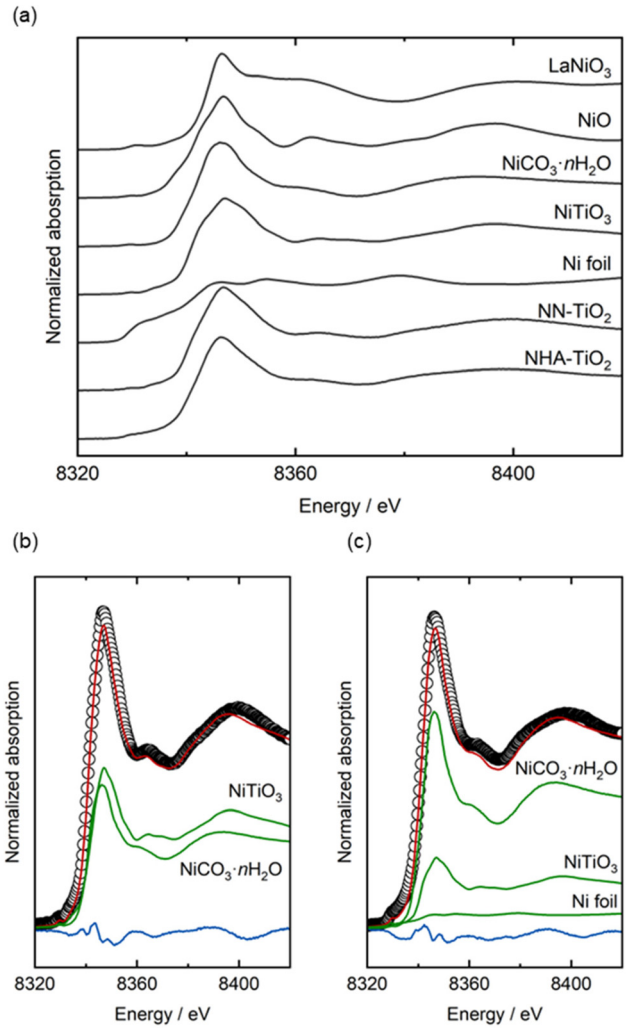

Fig. 5 (a) Normalized Ni-K edge XANES spectra of NN-TiO_2, NHA-TiO_2, Ni foil, $NiTiO_3$, $NiCO_3{\cdot}nH_2O$, NiO, and $LaNiO_3$. Linear combination fitting results of (b) NN-TiO_2 and (c) NHA-TiO_2. Raw data (black circle), fit curve (red line), residual curve (blue line), and fitted components (green) were shown.

XAFS spectra (Fig. 5a). The average oxidation states were estimated from the Ni K-edge energy at a normalised absorption of 0.2 (Fig. S5), yielding values of 2.0 for NHA-TiO_2 and 2.2 for NN-TiO_2. To further elucidate the composition, linear combination fitting was performed using all combinations of reference spectra of Ni, $Ni(OH)_2$, NiO, $NiTiO_3$, and $NiCO_3{\cdot}nH_2O$. In NN-TiO_2, $NiTiO_3$ was the predominant species (55%), followed by $NiCO_3{\cdot}nH_2O$ (45%) (Fig. 5b). Although carbonate including nickel species typically exhibit characteristic Raman bands at 1093 cm^{-1} (ν_1 symmetric stretch) and 1412/1440 cm^{-1} (ν_3 antisymmetric stretch),[31] these were absent in the Raman spectrum of NN-TiO_2 (Fig. 4), suggesting that the NiO_x species present adopts a local coordination environment similar to that of $NiCO_3{\cdot}nH_2O$ rather than a true carbonate phase. NiO_x is known to use as a dual cocatalyst for both H_2 and O_2 evolution *via* p–n junction formation with TiO_2,[32–34] though it typically exhibits low activity.[10,35] The suppressed photocatalytic performance observed for NN-TiO_2 may therefore derived from non-optimal interfacial binding of NiO_x and TiO_2. In contrast, NHA-TiO_2 comprised mainly $NiCO_3{\cdot}nH_2O$ (69%), with contributions from $NiTiO_3$ (24%) and metallic Ni (7%) (Fig. 5c), the latter arising from thermal self-reduction of the NHA nanoparticles. Given that XPS analysis revealed +2 oxidation state after heat-treatment (Fig. S2b), it is inferred that the Ni species in NHA-TiO_2 adopt a Ni/NiO_x composite structure. Such nanostructures have been reported to enhance photocatalytic activity.[36] In summary, the surface of NN-TiO_2 is dominated by inactive NiO_x species, which likely account for its diminished activity. In contrast, NHA-TiO_2 forms a composite nanostructure comprising rutile TiO_2, carbon, and Ni/NiO_x domains. The synergistic interplay among these nanoscale components is presumed to contribute to the enhanced H_2 evolution performance observed in NHA-TiO_2.

To optimise the photocatalytic system, the loading amount of NHA nanoparticles was systematically varied. The quantity of Ni species present after thermal treatment under an Ar atmosphere was assessed using XPS and X-ray fluorescence (XRF) analysis. As shown in Fig. 6a, XRF measurements revealed a linear correlation between nominal loading and Ni content. In contrast, XPS consistently indicated higher Ni amounts, suggesting preferential localisation of Ni species at the surface of the rutile TiO_2 nanoparticles, regardless of the overall loading. UV-visible diffuse reflectance (UV-Vis DR) spectra (Fig. 6b) showed increased absorption in especially

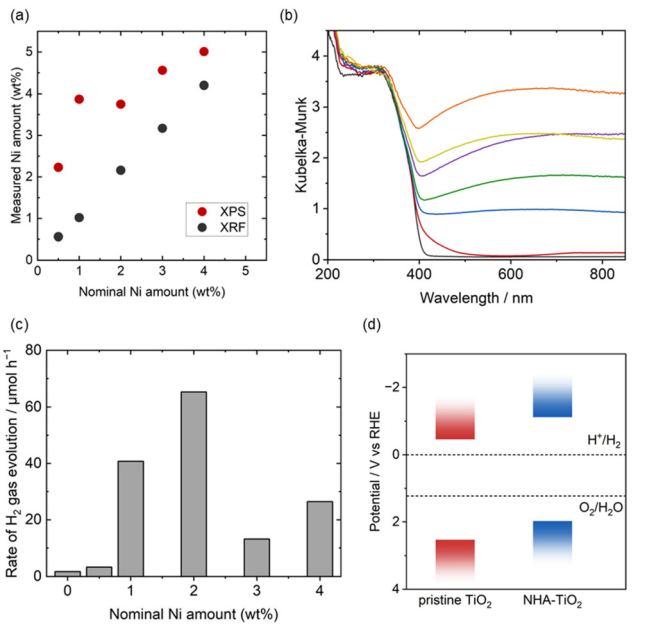

Fig. 6 (a) Measured Ni amounts by using XRF (black) and XPS (red). (b) UV-Vis-DR spectra of pristine-TiO_2 (black), NN-TiO_2 (red), NHA-TiO_2 with a nominal Ni amount of 0.5 (blue), 1.0 (green), 2.0 (purple), 3.0 (yellow), and 4.0 (orange). (c) Dependence of rates of H_2 evolution on the nominal Ni amount of NHA-TiO_2. (d) The potentials of CBM and VBM of pristine-TiO_2 (red) and NHA-TiO_2 (blue).

high wavelength region, a trend not observed in NN-TiO_2. These observations confirm that both Ni and carbon content increased proportionally with the amount of immobilised NHA nanoparticles. Photocatalytic H_2 evolution rates were then evaluated using the series of synthesised materials (Fig. 6c). Catalytic performance improved with increasing Ni content up to 2 wt%, beyond which a decline in activity was observed. This reduction is likely due to excessive light absorption by Ni and carbon species, which inhibits the generation of charge carriers upon photoexcitation. For reference, a benchmark experiment with 2 wt% Pt-loaded TiO_2 was also tested, which exhibited a H_2 evolution rate of 290 μmol h^{-1} (Fig. S6). Although this value significantly exceeds that of the best-performing NHA-TiO_2 sample, the latter demonstrates appreciable photocatalytic activity without reliance on noble metals, underscoring its potential as a sustainable cocatalyst. To further investigate the superior performance of NHA-TiO_2 at 2 wt% Ni loading, the potentials of the valence band maximum (VBM) and conduction band minimum (CBM) were estimated using UV-Vis spectroscopy, XPS, and electrochemical Mott–Schottky analysis (Fig. S7). Although the VBM potential relative to the vacuum level differed between pristine TiO_2 and NHA-TiO_2, their band gap energies were identical (Fig. S7(a) and (b)). The flat band potential of pristine-TiO_2 was comparable to the reported value,[37] whereas NHA-TiO_2 exhibited a lower potential (Fig. S7(c) and (d)). Since it has been reported that variations in surface states can lead to shifts in the flat-band potential,[38] it is reasonable to attribute the different flat-band potential of NHA-TiO_2 to the altered surface states. The results indicate a downward shift in the CBM of NHA-TiO_2 relative to pristine TiO_2 (Fig. 6d), which may facilitate more efficient H_2 evolution by promoting the generation of photo-excited electrons with greater reducing potential. Notably, XANES spectra of Ti K-edge, Ni K-edge, and Ni L-edge and pair distribution function (PDF) analysis showed that the chemical and structural states of NHA-TiO_2 remained largely unchanged after 3 h of photocatalytic testing (Fig. 7), with an oxidation state of 2.1 and composition of 62% of $NiCO_3{\cdot}nH_2O$, 36% of $NiTiO_3$, and 2% of Ni.

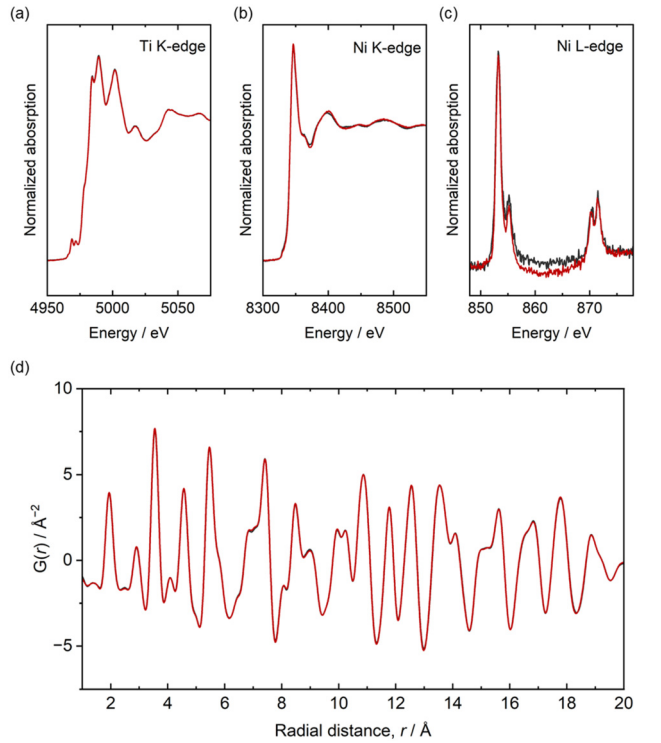

Fig. 7 (a) Ti K-edge, (b) Ni K-edge and (c) Ni L-edge XANES spectra, and (d) PDF patterns of NHA-TiO_2 before (black) and after (red) photocatalytic H_2 evolution.

Conclusions

In summary, we demonstrated a strategy for enhancing the photocatalytic H_2 evolution activity of rutile TiO_2 by immobilising NHA nanoparticles as thermally conversion cocatalyst precursors. Upon heat-treatment under an inert atmosphere, the NHA nanoparticles underwent thermal conversion to yield a composite surface structure comprising Ni/NiO_x and carbon nanodomains. Structural and spectroscopic analyses confirmed the formation of a sub-10 nm Ni-based cocatalyst onto the TiO_2 lattice. The presence of metallic Ni was unique to the NHA-derived system and was implied to form Ni/NiO_x composite structures, which remained stable during photocatalytic testing. These nanostructures, along with co-deposited carbon, synergistically enhanced the H_2 evolution rate, achieving a 37-fold improvement compared to pristine TiO_2 under UV irradiation. In contrast, a reference sample prepared using Ni$(NO_3)_2$ exhibited suppressed activity, likely due to the formation of inactive NiO_x species with poor interfacial contact. Furthermore, optimisation of the cocatalyst loading revealed a volcano-type trend, with a maximum activity at 2 wt% Ni. The VBM and CBM analysis indicated a downward shift of the CBM, which is favourable for the photocatalytic H_2 evolution reaction. This work presents a versatile approach to designing noble-metal-free photocatalytic systems through rational control of thermal conversion pathways and nanostructure formation at the semiconductor surface.

Methods

Materials

Nickel chloride hexahydrate ($NiCl_2{\cdot}6H_2O$, 98.0%) and acrylic acid (99%) were purchased from Sigma-Aldrich Co., LLC (St Louis, MO, USA). Nickel nitrate hexahydrate (Ni$(NO_3)_2{\cdot}6H_2O$, 99%), propylene oxide (99%), methanol (99%), and ethanol (99.5%) were purchased from FUJIFILM Wako Pure Chemical Corp. (Osaka, Japan). Reference catalyst of JRC-TIO-16 was purchased from Catalysis Society of Japan Ultrapure water with a resistivity of 18.2 MΩ cm was used in all experiments. All the reagents were used as received.

Synthesis of NHA nanoparticles

$NiCl_2{\cdot}6H_2O$ (2.5 mmol) and acrylic acid were dissolved in 5.0 mL of ethanol. Propylene oxide was added under stirring. Obtained homogenous solutions, including reagents with a molar ratio of $NiCl_2{\cdot}6H_2O$: acrylic acid : propylene oxide = 1 : 2 : 15, were left in water bath with a controlled temperature of 25 °C for 24 h. The resultant dispersions were rotary evaporated at 30 °C under 30 kPa for 15 min to remove residual propylene oxide and quench the reaction. Finally, the concentration of dispersion (metal basis) was set as 0.5 mol L^{-1} by adding ethanol.

Photocatalyst preparation

The powder of JRC-TIO-16 was heat-treated at 873 K for 2 h with a ramp rate of 10 K min^{-1}. Heat-treated JRC-TIO-16 (470.4 mg) was suspended in the 1.6 mL of NHA nanoparticle dispersion (including 9.6 mg of Ni (metal basis)) and 2.2 mL of water. The weight ratio of TiO_2 : Ni equals to 0.98 : 0.02. The amount of NHA nanoparticle dispersion was changed to tune the amount of immobilized Ni species. Obtained suspension was ultrasonicated for 2 min and allowed drying the solvent on a hot water (353 K). Dried powders were heat-treated at 873 K for 1 h with a ramp rate of 10 K min^{-1} under Ar atmosphere. For a comparison, aqueous solution of nickel nitrate (42 mmol L^{-1}) was used instead of NHA nanoparticle dispersions to prepare $Ni(NO_3)_2$ immobilized TiO_2 precursor. Obtained suspensions were dried and heat-treated with a same condition written above. Pt-loaded TiO_2 were prepared by pohotodeposition method as described in the reported studies.[19,39]

Photocatalytic activity measurement

Photocatalytic H_2 evolution half reaction was carried out in a Pyrex top-irradiation vessel connected to a glass closed gas circulation system. A 100 mg of cocatalysts-loaded TiO_2 powders were dispersed in 100 mL of mixed solvent (water : methanol = 0.9 : 0.1 in volume) using a magnetic stirrer. The reactant solution was evacuated under vacuum several times to completely remove any residual air. Then, a small amount of Ar gas (*ca.* 20 kPa) was introduced into the reaction system prior to irradiation under a 300 W xenon lamp with an output current of 20 A. The water filter was set at the top of the reaction cell to avoid heating the reaction system by light irradiation. The reactant solution was maintained at 293 K by a water bath during the reaction. The evolved gases were analysed by gas chromatography (Shimadzu, GC-8A with thermal conductivity detector and MS-5A column, argon carrier gas).

Characterization

X-ray diffraction (D2 PHASER, Bruker AXS, Karlsruhe, Germany) with Cu Kα radiation was employed to determine the crystal phases and lattice constants of the samples. Raman spectroscopy (NRS-4500, JASCO, Tokyo, Japan) were used to analyse chemical bonding. Ultraviolet–visible spectroscopy (V-750, JASCO, Tokyo, Japan) equipped with diffuse reflectance unit was used to investigate the band gap of the powder samples. The shape, size, crystallinity, and chemical composition of samples were observed by using transmission electron microscopy (JEM-2010, JEOL, Tokyo, Japan) and scanning transmission electron microscopy (JEM-2100F, JEOL, Tokyo, Japan) equipped with energy dispersive spectroscopy (DrySD 60GV detector, JEOL, Tokyo, Japan, combined with a Thermo Fischer Scientific NORAN System 7, Thermo Fischer Scientific, Massachusetts, USA). The transmission electron microscopy images were collected using an accelerating voltage of 200 kV. X-ray fluorescence (XRF) measurements were conducted to determine the chemical compositions of samples using a 5 μm thick Mylar film window. The spectrum-imaging (SI) datasets were collected in a synchronized STEM mode and electron energy loss spectroscopy (EELS) using a Gatan Continuum S spectrometer equipped on a JEOL JEM-2100F TEM. The STEM-EELS SI datasets were acquired in the dual-EELS mode with camera length of 30 mm, spectrometer entrance aperture size of 5 mm, collection semi-angle of 20 mrad and energy resolution (full width at half maximum of zero-loss peak) of 1.0 eV. The dual-EELS mode acquires the low-loss and core-loss EELS spectra almost simultaneously. The STEM-EELS SI acquisition and data analyses were carried out using the Gatan Microscopy Suite (GMS) of version 3.6. The obtained EELS-SI dataset was aligned by the zero-loss peak. A power-law background model was used. The multiple linear least square (MLLS) fitting routine available in the GMS 3.6 software package was used to obtain the intensity map. XPS spectra were obtained using an ESCA-3400 (Shimadzu) instrument equipped with a monochromatic Mg Kα source (150 W). The binding energy values were corrected using that of the C 1s peak (284.8 eV) as an internal reference, which is the signal from surface contaminated hydrocarbons. High-energy X-ray total scattering measurements were carried out at the BL04B2 beamline of SPring-8 (Japan) using incident X-rays at 112.8 keV (2θ = 0.2–24.0°, Q = 0.18–23.8 $Å^{-1}$) with the automated system.[40] Data normalization to Faber–Ziman structure factors $S(Q)$ and transformation to pair distribution functions $g(r)$ were performed using standard procedures and PDFgui software.[41] XAFS measurements at the Ti and Ni K-edges were conducted in transmission mode at BL01B1 (SPring-8, Japan). Soft-X-ray XAFS measurements were carried out at BL27SU (SPring-8, Japan) for XANES region of Ni L-edge. Spectra were calibrated using metal foils and analysed with Demeter software.[42] Normalized absorption XANES spectra were obtained by subtracting atomic absorption backgrounds *via* cubic spline interpolation.

Electrochemical measurements

All electrochemical measurements were carried out in a conventional three-electrode cell configuration with 0.5 mol L^{-1} H_2SO_4 aqueous solution as the electrolyte at a room temperature. A platinum wire and Ag/AgCl (filled with saturated KCl aqueous solution) were used as the counter electrode and the reference electrode, respectively. The cocatalyst-modified TiO_2 particles were suspended in ethanol, deposited on the F-doped tin oxide coated glass substrate, and dried at 398 K using

temperature controlled hot-plate. Mott–Schottky plot was obtained by using the potential range, where the faradaic reaction does not occur. The potential *versus* reverse hydrogen electrode, E_{RHE}, was calculated as $E_{Ag/AgCl} + 0.059 \times pH + 0.199$, where $E_{Ag/AgCl}$ was measured potential.

Determination of band edge positions

The potentials of the VBM and CBM were estimated using UV-Vis, XPS, and electrochemical Mott–Schottky analysis. The potential of the VBM relative to the vacuum level, $E_{VBM/vacuum}$, was obtained by extrapolating the XPS spectra. The potential of the CBM relative to the vacuum level, $E_{CBM/vacuum}$, was calculated from the band gap energy, E_g, estimated by the Tauc plot of the UV–Vis spectra, according to $E_{CBM/vacuum} = E_{VBM/vacuum} - E_g$. The flat band potential, E_{fb}, was considered to represent the Fermi level in aqueous solution. Accordingly, the potentials of the VBM and CBM relative to the reversible hydrogen electrode, E_{VBM} and E_{CBM}, were calculated as $E_{VBM} = E_{VBM/vacuum} + E_{fb}$ and $E_{CBM} = E_{CBM/vacuum} + E_{fb}$.

Author contributions

NT: writing – original draft, conceptualization, funding acquisition, methodology, supervision; RN: investigation, analysis; KK: methodology, supervision; KI: supervision; SI, HY, TI: analysis; YO: supervision.

Conflicts of interest

There are no conflicts to declare.

Data availability

The data supporting this article, lattice constants, SEM images, STEM-EELS analysis, XPS analysis, XAFS analysis, H_2 evolution rate, Tauc plot and Mott-Schottky plot have been included as part of the SI.

Supplementary information is available. See DOI: **https://doi.org/10.1039/d5nr02166a**.

Acknowledgements

This work was partially supported by JSPS KAKENHI (Grant Numbers JP22H05142, JP22H05143, JP23H00236, and JP25K01859) and JST FOREST Program Grant Number JPMJFR221 W. We also thank MEXT Strategic Professional Development Program for Young Researchers (HIRAKU-Global), and the Cooperative Research Program of the facilities of the Institute of Materials and Systems for Sustainability, Nagoya University. Synchrotron radiation experiments were performed at the SPring-8 facility under proposals 2024A1258, 2024A1898, 2025A1252, and 2025A1432. The authors thank the beamline staff for their technical assistance during the measurements. The XAFS data of $NiTiO_3$, and $NiCO_3{\cdot}nH_2O$ are utilized by SPring-8 BENTEN database.[43]

References

1 S. Nishioka, F. E. Osterloh, X. Wang, T. E. Mallouk and K. Maeda, *Nat. Rev. Methods Primers*, 2023, **3**, 42.
2 J. H. Kim, D. Hansora, P. Sharma, J. W. Jang and J. S. Lee, *Chem. Soc. Rev.*, 2019, **48**, 1908–1971.
3 M. A. Abdelkareem, A. A. Abdelghafar, M. Mahmoud, E. T. Sayed, M. S. Mahmoud, A. H. Alami, M. M. A. Agha and A. G. Olabi, *Sol. Energy*, 2023, **265**, 112072.
4 A. Fujishima and K. Honda, *Nature*, 1972, **238**, 37–38.
5 T. Takata, J. Jiang, Y. Sakata, M. Nakabayashi, N. Shibata, V. Nandal, K. Seki, T. Hisatomi and K. Domen, *Nature*, 2020, **581**, 411–414.
6 Y. Sasaki, H. Nemoto, K. Saito and A. Kudo, *J. Phys. Chem. C*, 2009, **113**, 17536–17542.
7 K. Maeda, K. Teramura, D. Lu, N. Saito, Y. Inoue and K. Domen, *J. Phys. Chem. C*, 2007, **111**, 7554–7560.
8 A. Nakada, T. Uchiyama, N. Kawakami, G. Sahara, S. Nishioka, R. Kamata, H. Kumagai, O. Ishitani, Y. Uchimoto and K. Maeda, *ChemPhotoChem*, 2018, **3**, 37–45.
9 M. Hara, J. T. Lean and T. E. Mallouk, *Chem. Mater.*, 2001, **13**, 4668–4675.
10 C. C. L. McCrory, S. Jung, J. C. Peters and T. F. Jaramillo, *J. Am. Chem. Soc.*, 2013, **135**, 16977–16987.
11 F. Zhang, A. Yamakata, K. Maeda, Y. Moriya, T. Takata, J. Kubota, K. Teshima, S. Oishi and K. Domen, *J. Am. Chem. Soc.*, 2012, **134**, 8348–8351.
12 A. Iwase, S. Yoshino, T. Takayama, Y. H. Ng, R. Amal and A. Kudo, *J. Am. Chem. Soc.*, 2016, **138**, 10260–10264.
13 G. G. C. Arizaga, K. G. Satyanarayana and F. Wypych, *Solid State Ionics*, 2007, **178**, 1143–1162.
14 S. Nakagaki, G. S. Machado, J. F. Stival, E. Henrique dos Santos, G. M. Silva and F. Wypych, *Prog. Solid State Chem.*, 2021, **64**, 100335.
15 K. Maeda, T. Motohashi, R. Ohtani, K. Sugimoto, Y. Tsuji, A. Kuwabara and S. Horike, *Sci. Technol. Adv. Mater.*, 2024, **25**, 2416384.
16 N. Tarutani, S. Kimura, T. Sakata, K. Suzuki, K. Katagiri and K. Inumaru, *ACS Mater. Lett.*, 2022, **4**, 1430–1435.
17 N. Tarutani, Y. Hiragi, K. Akashi, K. Katagiri and K. Inumaru, *Nanoscale*, 2023, **15**, 15656–15664.
18 N. Tarutani, K. Akashi, K. Katagiri and K. Inumaru, *Inorg. Chem.*, 2023, **62**, 13977–13984.
19 K. Maeda, N. Murakami and T. Ohno, *J. Phys. Chem. C*, 2014, **118**, 9093–9100.
20 K. Maeda, *Chem. Commun.*, 2013, **49**, 8404–8406.
21 N. Tarutani, Y. Tokudome, M. Jobbágy, G. J. A. A. Soler-Illia, Q. Tang, M. Müller and M. Takahashi, *Chem. Mater.*, 2018, **31**, 322–330.
22 K. Domen, S. Naito, T. Onishi, K. Tamaru and M. Soma, *J. Phys. Chem.*, 1982, **86**, 3657–3661.

23 S. P. S. Porto, P. A. Fleury and T. C. Damen, *Phys. Rev.*, 1967, **154**, 522–526.
24 J. C. Parker and R. W. Siegel, *J. Mater. Res.*, 2011, **5**, 1246–1252.
25 J. C. Parker and R. W. Siegel, *Appl. Phys. Lett.*, 1990, **57**, 943–945.
26 F. Tuinstra and J. L. Koenig, *J. Chem. Phys.*, 1970, **53**, 1126–1130.
27 M. A. Pimenta, G. Dresselhaus, M. S. Dresselhaus, L. G. Cançado, A. Jorio and R. Saito, *Phys. Chem. Chem. Phys.*, 2007, **9**, 1276–1290.
28 N. Tarutani, M. Asanome, K. Okada, M. Takahashi, T. Minato, M. Sadakane, K. Katagiri and K. Inumaru, *J. Ceram. Soc. Jpn.*, 2023, **131**, 830–836.
29 S. K. Parayil, H. S. Kibombo, C.-M. Wu, R. Peng, J. Baltrusaitis and R. T. Koodali, *Int. J. Hydrogen Energy*, 2012, **37**, 8257–8267.
30 Y. Deligiannakis, E. Bletsa, E. Mouzourakis, M. Solakidou and K. Adamska, *ACS Appl. Nano Mater.*, 2024, **7**, 11621–11633.
31 R. L. Frost, M. J. Dickfos and B. Jagannadha Reddy, *J. Raman Spectrosc.*, 2008, **39**, 1250–1256.
32 M. Wang, Y. Hu, J. Han, R. Guo, H. Xiong and Y. Yin, *J. Mater. Chem. A*, 2015, **3**, 20727–20735.
33 T. Sreethawong, Y. Suzuki and S. Yoshikawa, *Int. J. Hydrogen Energy*, 2005, **30**, 1053–1062.
34 S.-i. Fujita, H. Kawamori, D. Honda, H. Yoshida and M. Arai, *Appl. Catal., B*, 2016, **181**, 818–824.
35 M. Okazaki, Y. Yamazaki, D. Lu, S. Nozawa, O. Ishitani and K. Maeda, *Chem. Catal.*, 2025, **5**, 101167.
36 M. Abudukade, M. Pinna, D. Spanu, G. De Amicis, A. Minguzzi, A. Vertova, S. Recchia, P. Ghigna, G. Mul and M. Altomare, *J. Phys. Chem. C*, 2024, **128**, 16020–16031.
37 G. Cooper, J. A. Turner and A. J. Nozik, *J. Electrochem. Soc.*, 1982, **129**, 1973–1977.
38 H. Ge, H. Tian, Y. Zhou, S. Wu, D. Liu, X. Fu, X. M. Song, X. Shi, X. Wang and N. Li, *ACS Appl. Mater. Interfaces*, 2014, **6**, 2401–2406.
39 B. Kraeutler and A. J. Bard, *J. Am. Chem. Soc.*, 1978, **100**, 4317–4318.
40 H. Yamada, K. Nakada, M. Takemoto and K. Ohara, *J. Synchrotron Radiat.*, 2022, **29**, 549–554.
41 C. L. Farrow, P. Juhas, J. W. Liu, D. Bryndin, E. S. Bozin, J. Bloch, T. Proffen and S. J. Billinge, *J. Phys.:Condens. Matter*, 2007, **19**, 335219.
42 B. Ravel and M. Newville, *J. Synchrotron Radiat.*, 2005, **12**, 537–541.
43 H. Ofuchi, T. Matsumoto and T. Honma, *Radiat. Phys. Chem.*, 2024, **218**, 111581.